AIAA SciTech Forum
9 - 13 January 2017, Grapevine, Texas
55th AIAA Aerospace Sciences Meeting

10.2514/6.2017-0038

Near Field Sonic Boom Analysis with HUNS3D Solver

Boping Ma[1], Gang Wang[2,*], Jiong Ren,[3] Ye Zhengyin[4]
Dept. of Fluid Mechanics, School of Aeronautics,
Northwestern Polytechnical University, Xi'an 710072, China

Gecheng Zha[5]
Dept. of Mechanical and Aerospace Engineering, University of Miami, Coral Gables, FL33124

Accurate analysis of sonic boom pressure signature using Computational Fluid Dynamics (CFD) is still a challenging task. In this paper, four benchmark cases including two axisymmetric body, a simple delta wing body and a full configuration includes fuselage, wing, tail, flow-through nacelles, and blade wing were computed with a Reynold-averaged Navier-Stokes (RANS) based flow solver to predicted the near field sonic boom signature. The computed results from CFD agree well with the measured data in wind tunnel experiment. The effects of geometry equivalent radius, grid size, turbulence model and spatial discretization schemes are investigated and discussed.

I. Introduction

FOR centuries, people have been seeking for approaches to travel faster and safer. With the development of modern aircraft design method, supersonic flight has been commonly applied in military aircrafts. Whereas the supersonic flights over land by civil aircraft are currently prohibited in many countries. One of the main constrains on expected new-generation supersonic transports is sonic boom, a huge noise phenomenon caused by shock waves. It is challenging to theoretically predict how sonic boom signatures are during its propagation, and finally on the ground, because of the long travel distance, the existence of the Earth's turbulent boundary layer, the atmosphere inhomogeity and even molecular relaxation.[1] Hence, modern sonic boom prediction is usually divided into two steps. The pressure waveform in the boundary of the near field is firstly obtained by wind tunnel or numerical experiments, then the final boom effect on the ground or elsewhere is predicted by quasi-linear theory derived from Whitham,[2] or the methods originated from nonlinear Burger's equation.[3-5]

An near-result extrapolation step as well as a matching one was often added between the near and far field procession in the early days.[6, 7] Siclary et al[8] and Page et al[9] successfully introduced CFD based on Euler equation to obtain near field pressure in early 1990s, while Cliff et al[10] used unstructured tetrahedral grids and made several compilations which shown acceptable correlations. Jones et al[11] introduced Navier-Stocks equation instead of Euler equations to catch the viscosity details of the near field shock waves in 2006. After then, CFD near field sonic boom prediction has become more accurate and seem able to consistent with tunnel results more. NASA has organized several sonic boom workshops since early 1990s. The latest one was held in the autumn of 2008 to evaluate NASA's capability to predict both the near and far field signatures of variant geometries.[12] The results from AIRPLANE, Cart3D, FUN3D, and USM3D etc. flow solvers were evaluated in the workshop. The workshop evaluated the accuracy of available method and gave remarkable lessons to the 1st AIAA Sonic Boom Prediction Workshop (SBPW-1) held on January 11, 2014.[13] The objective of SBPW-1 was to assess the state of the art of predicting near field pressure signatures needed for accurate and reliable sonic boom prediction. There were approximately 50 attendees from 7 nations. The participants utilized a series of uniformly refined workshop provided grids and self-generated grid for computing solutions on the provided geometries.

Meanwhile, some different trial has made progresses. Yamashita and Suzuki[14] presented a full-field sonic boom simulation approach, in which the whole flow field including both the zone around a supersonic body and that on the ground is analyzed as a single computational domain. The computed sonic boom propagation is in

[1]Ph.D. Candidate, School of Aeronautics, Dept. of Fluid Mechanics, Email: bopingma@mail.nwpu.edu.cn, AIAA student Member
[2]Associate Professor, School of Aeronautics, Dept. of Fluid Mechanics, Email: wanggang@nwpu.edu.cn, AIAA Member
[3]Ph.D. Candidate, School of Aeronautics, Dept. of Fluid Mechanics, Email: rensj6962@163.com
[4]Professor, School of Aeronautics, Dept. of Fluid Mechanics, Email: yezy@nwpu.edu.cn
[5]Professor, Dept. of Mechanical and Aerospace Engineering, Email: gzha@miami.edu, AIAA Associate Fellow
[*]Corresponding Author

good agreement with that by the two-steps method and conforms to the flight test results. To improve the prediction accuracy of CFD approach, many efforts have been made to near field grid adaptation.[15-19] The influence of viscous effects, turbulence models and higher order schemes has also been investigated.[20, 21]

In this paper, four benchmark cases including two axisymmetric body, a simple delta wing body and a full configuration includes fuselage, wing, tail, flow-through nacelles, and blade wing were computed with a RANS based flow solver to predicted the near field sonic boom signature. The influences of geometry tip rounding, grid size, turbulence model and spatial discretization schemes are investigated. The results from CFD have been compared with the measured data in wind tunnels. In the rest of this paper, the CFD approach and mesh generation method used in this paper is described in section II. The results of simulation and discussions will be present in section III. A brief conclusion will be drawn in section IV.

II. Numerical Method

A. CFD Solver

The simulations in this paper are performed with an in-house hybrid unstructured RANS solver named HUNS3D.[22] In HUNS3D, the non-dimensional governing equations are discretized with the cell-centered finite-volume method on unstructured hybrid meshes composed of hexahedrons, prisms, tetrahedrons, and pyramids. Several upwind including ROE[23], AUSM series[24] and Entropy-consistent (EC) schemes[25] and central[26] convective flux discretization schemes are available in this flow solver. And the linear interpolation was used to improve the calculation accuracy. Venkatakrishnan slope limiter[27] is equipped with all above upwind schemes to preserve the total variation diminishing (TVD) property and guarantee the monotone solutions in all latter numerical simulations. The semi-discretized equations are integrated implicitly by the backward Euler method together with the Lower-Upper Symmetric-Gauss-Seidel (LU-SGS) scheme. A range of turbulence models are available in HUNS3D code, including the one-equation Spalart-Allmaras (SA) model[28], Menter's two-equation shear stress transport (MSST) $k-\omega$ model[29], and hybrid RANS-LES model.

The integral form of RANS equations enclosed with the SA turbulence model for a control volume Ω can be written as follows:

$$\frac{\partial}{\partial t}\int_{\Omega}\mathbf{W}d\Omega+\oint_{\partial\Omega}(\mathbf{F}_c-\mathbf{F}_v)\cdot\vec{n}dS=\int_{\Omega}\mathbf{Q}_{source}d\Omega \tag{1}$$

where $\mathbf{W}=\left[\rho \quad \rho u \quad \rho v \quad \rho w \quad \rho E \quad \rho\tilde{v}\right]^{\mathrm{T}}$ is the vector of conserved quantities with $\rho,u,v,w,E,$ and $\tilde{v}$ denoting the density, Cartesian velocity components, specific total energy, and working variables of the SA turbulence model, respectively. The source term $\mathbf{Q}_{source}=\left[0 \quad 0 \quad 0 \quad 0 \quad 0 \quad Q_T\right]^{\mathrm{T}}$ only lies in turbulence model equation, where Q_T repents the source term of the SA turbulence model. $\mathbf{F}_c$ and $\mathbf{F}_v$ comprise the convective and viscous flux vectors, respectively. Their detailed form can be found in Ref. [30]. The spatial discretization and time-integration of the turbulence model equation and mean flow equation are conducted in a loosely coupled way; hence, the turbulence model equation can be easily solved by using the same algorithms as the flow equations.

B. Mesh Strategy

Lots of work have been done to investigate the influence of mesh generation method to the accuracy of sonic boom prediction and beneficial conclusions have been concluded. A detailed description can be found in Ref.[31]. In present work, Advancing-Front method was used to generate the volume mesh of the inner cylinder wall and Inflate Generation method used to provide the aligned anisotropic cells for all tested configurations.

Fig. 1a shows a schematic of the inner cylindrical mesh of the LM1021 configuration. Based on the provided geometry and mesh, hybrid unstructured mesh with 24,805,540 cells, 12,144,918 volume nodes, 252741 surface node points and 33 layers of prism mesh in boundary layer has been generated for viscous computations. To reduce the dissipative effects, the model was placed closed to the aligned grids within the non-aligned inner-cylinder mesh (as shown in Fig. 1b). Furthermore, more nodes was placed in the horizontal line of the cylinder to make better transition from the non-aligned region to the aligned cells.

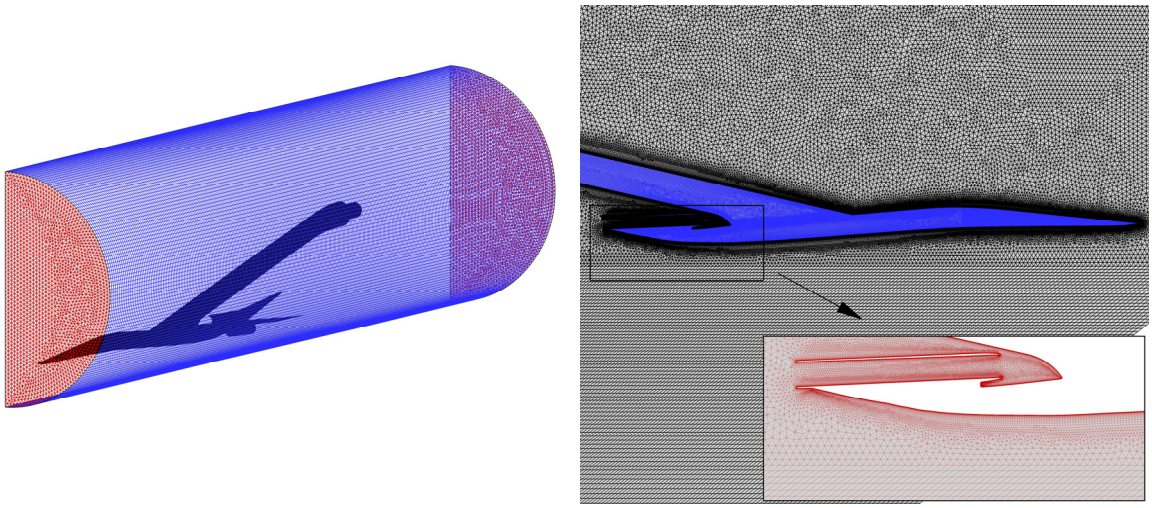

(a) Inner body of LM1021 (b) Details of transition of inner and inflated grid

Fig. 1 Geometry and computation zone of LM1021

III. Result and Discussions

A. NASA Cone Model

The NASA cone model tested here is from the NASA sonic boom wind tunnel testing.[32] As shown in fig. 2a, the half cone angle is 3.24° and the length is 2 inches (5.08 cm). It had been tested in several Mach numbers for its near field sonic boom signature in the wind tunnel test. Hybrid unstructured mesh has been generated for a half cone model and the computational domain size is shown in fig. 2b. The available NASA Langley 4- by 4-foot supersonic pressure tunnel validation data for this test case are H=20, 30 and 40 in. off the centerline pressure at $M_\infty = 2.01$ and $\alpha = 0°$.

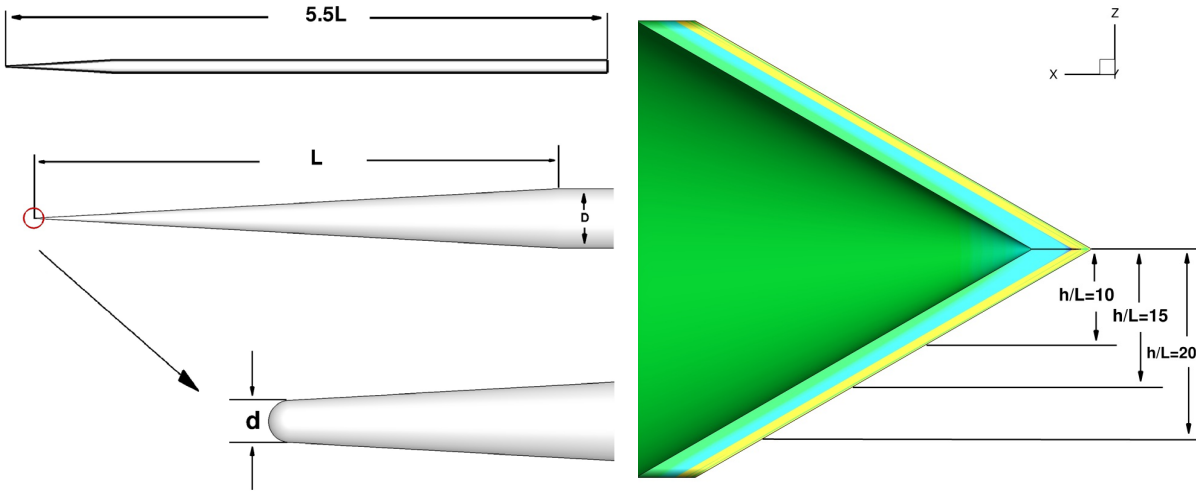

(a) NASA Cone model (b) Computation zone and signal extraction position

Fig. 2 Geometry and computation zone of NASA Cone model

In the wind tunnel test, the model has a sharp tip, whereas in the mesh generation process, the tip needs to be modified to attain the grid quality. To investigate the influence of geometry sensitivity of the rounding parameters, several meshes have been generated based on the modified model with various equivalent radius, and the simulation results is shown in fig. 3. It is clear that the different equivalent radius in the tip causes a difference in the capture of the shock wave and expansion wave. The pressure signature with smaller radius agrees better with the experimental data in the front shock wave position than others, and the pressure signature is under predicted in the main expansion portion.

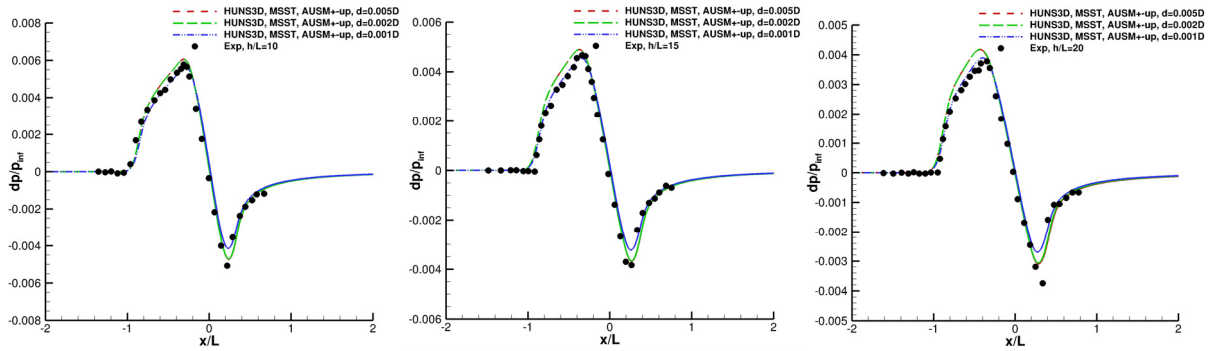

(a) *h/L*=10 **(b) *h/L*=15** **(c) *h/L*=20**

Fig. 3 NASA Cone, experimental data compared with HUNS3D computations, M_∞=2.01, α=0°, *Re*=3.75×10^5

Comparison between the experimental measured data with calculation of the NASA Cone configuration with various discretization schemes are shown in fig. 4. The red dash line denotes the result with AUSM+-up scheme, the green dash-dot line denotes that with central scheme and the blue dash-dotted line denotes that with ROE scheme. The HUNS3D viscous computations were performed at a Mach number of 2.01 and a Reynolds number of 3.75×10^5 per inch. The turbulence used here is MSST model.

Fig 4a-c are computations of the pressure signature at 20-, 30-, and 40-inch altitudes, respectively. It can be seen that all the schemes capture the shock wave and expansion wave position accurately, even at a greater distance (h=40 inches) from the model as shown in fig 4c, which represents an *h/L* of 20 with respect to the length of the model. The main difference of the three schemes is that the Roe scheme seems to perform better in capturing the beginning of the shock wave than others. The central scheme would capture a small depression in all these condition. In addition, the captured peak values of expansion wave with these three schemes are also different, results with the Roe scheme is greater than the others. Overall, the Roe scheme has superiority for the NASA cone model than AUSM+-up and central schemes, which due to less numerical dissipation of Roe scheme than other two schemes.

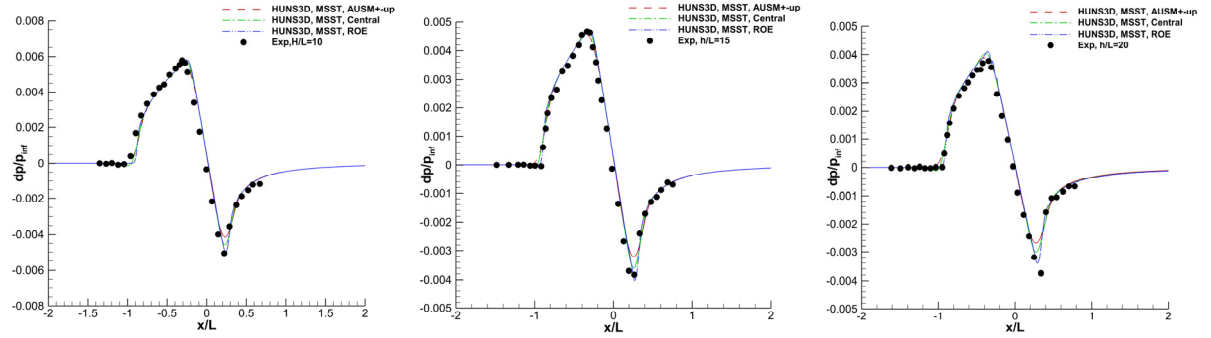

(a) *h/L*=10 **(b) *h/L*=15** **(c) *h/L*=20**

Fig. 4 NASA Cone, experimental data compared with HUNS3D computations, M_∞=2.01, α=0°, *Re*=3.75×10^5

B. SEEB-ALR Model

The axisymmetric Seeb-ALR model, as a required model in SBPW-1 workshop, was constructed by Lockheed Martin and was tested in the NASA Ames 9×7 ft. Supersonic Tunnel in 2012.[33] The model is a body of revolution based upon the work of Darden, George and Seebass.[34] The "ALR" moniker denotes "Aft Lift Relaxation" which is a design feature that increases the diameter of the geometry slightly to reach a maximum just aft of the shoulder, and then tapers slightly to meet the cylindrical sting extension. Traditional Seeb designs transition to the cylindrical aft-bodies monotonically. The Seeb-ALR solid model is constructed in the siemens PLM software NX computeraided design tool from a STEP file of the scanned, as-built wind tunnel model. The geometry differences between the as-designed and as-built are summarized by Cliff et al.[35], Aftosmis and Nemec.[36] The model has a reference length of L= 17.68 in. This axisymmetric calibration model should theoretically produce a flat top pressure signature with an 8-inch region of constant pressure. It was designed to help assess the accuracy of the experimental pressure signatures.

The SBPW-1 workshop provides several types of grid, one of which deals with the sharp tip with a cut plane, as shown in fig. 5a. Based on the given geometry a hybrid unstructured mesh is generated. The mesh is inclined at the Mach angle to resolve the oblique shock waves, the computation zone is shown as fig. 5b. The available NASA

Ames wind tunnel validation data for this test case are h=21.2 and h=42.0 in. off the centerline pressure extraction at $M_\infty = 1.6$ and $\alpha = 0°$.

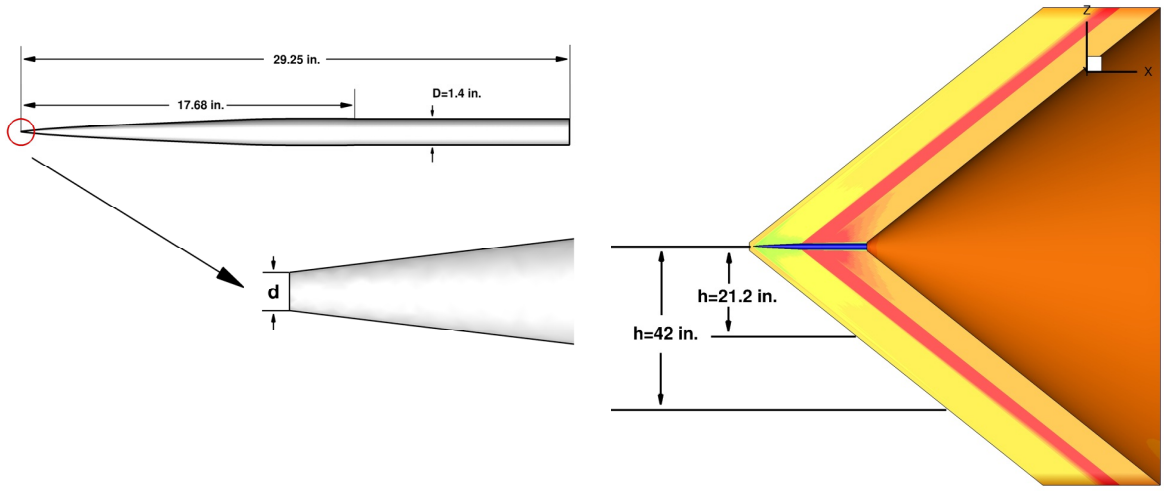

(a) Geometry of Seeb-ALR **(b) Computation Zone and signal extracted position**

Fig. 5 Geometry and computation zone of Seeb-ALR

Experimental pressure signatures at the distance of h=21.2 in. and h=42 in. from the model are compared with HUNS3D turbulent flow solutions as follows.

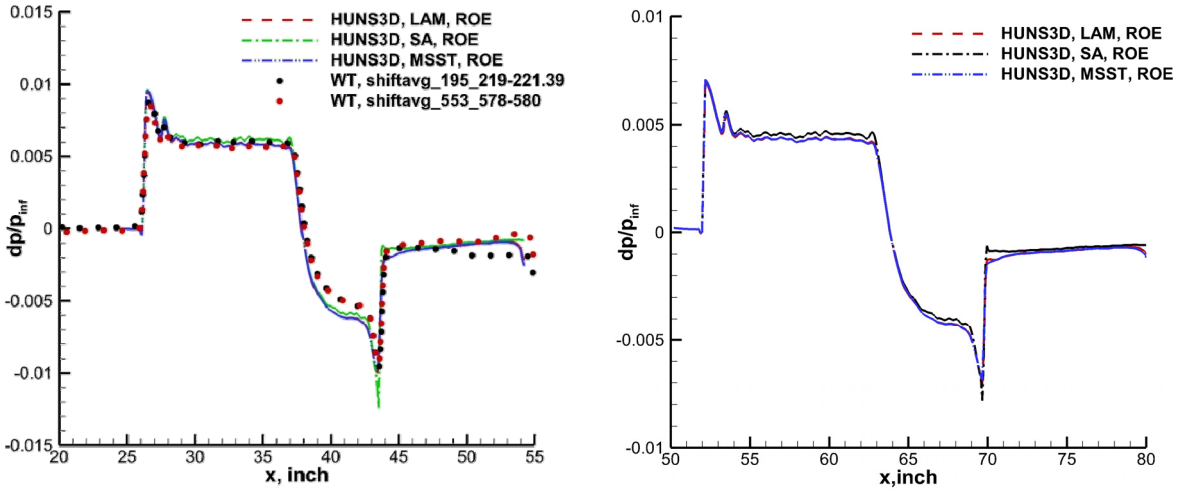

(a) h=21.2 in. **(b) h=42 in.**

Fig. 6 Seeb-ALR, experimental data compared with HUNS3D computations, M_∞=1.6, α=0°, *Re*=3.75×10^5

Fig. 6 show the comparisons between the experimental data and viscous simulations with different turbulent models. The calculation is performed at the Mach number of 1.6, angle of attack of 0 and the Reynolds number of 3.75×10^5 per inch. Fig. 6(a) compares two repeat experimental runs, one taken at the start of the wind tunnel test and the other mid-way through the test, with the laminar flow computations, SA turbulence model result as well as MSST model computation result. There are good agreement between the computations and experiment. The solution with laminar flow is very similar with that of the MSST turbulence model. The solution with SA turbulence model performs well in capturing the shock wave and expansion wave, however, the main expansion is a little over predicted. The saw teeth oscillation at the flat top resulting from the 2nd order derivative oscillation of the geometry is very well captured in all these conditions. In this case, the laminar flow and the MSST turbulence model results improve the comparison with the experiment in the forward flat pressure region, but results in poorer expansion region of the aft portion. Fig. 6(b) shows the results at h=42 in., which also accords with above conclusions.

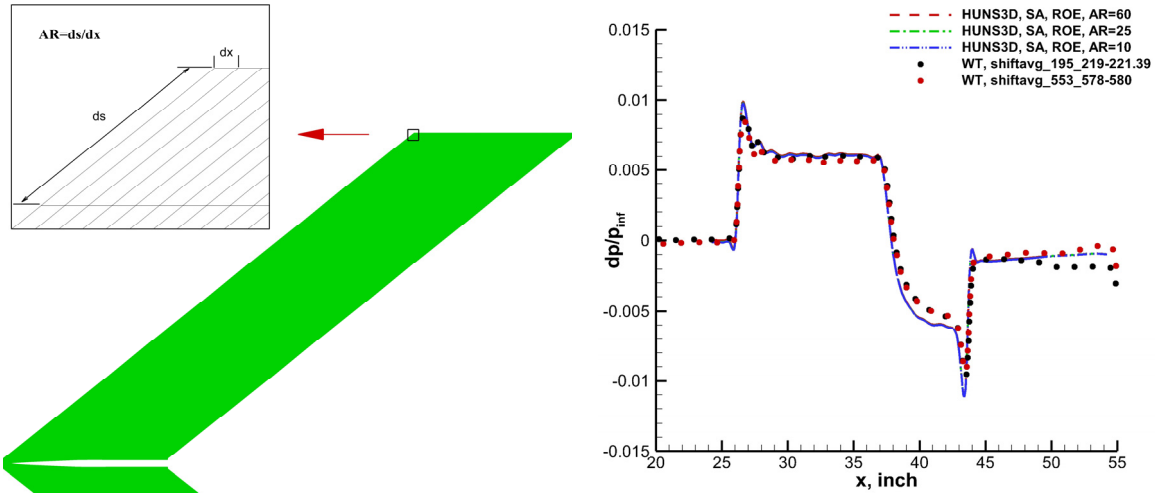

(a) Aspect ratio (AR) definition **(b) h=21.2 in.**

Fig. 7 Seeb-ALR, experimental data compared with HUNS3D computations with different ARs, M_∞=1.6, α=0°, Re=3.75×10^5

In Fig. 7, we give results from a series of grid with different aspect ratio in the farfield domain. The mesh elements increase from 7,334,863 to 19,483,963 as AR decreases from 60 to 10. There are very slightly differences in the strength of the captured shock wave and expansion wave. The peak value of the first and second shock wave pressures show sensitivity to AR, decreasing AR would give lower value of overpressure. In fact, the lower AR represents the denser grid and the less numerical dissipation, so the higher accuracy will be achieved in the calculation. This easily leads to unphysical oscillations near shock waves or the over/undershoot values at the peak points.

C. 69º Delta Wing-Body Model

Originally identified as "Model 4" in the 1973 wind tunnel study by Hunton and Hicks et al.,[37] the 69° delta-wing-body (DWB) is also a axisymmetric model. It has a fuselage and diamond airfoil wing configuration. As shown in fig. 8, the model has a reference length of 17.52 in.. The wing thickness to chord ratio is 0.05 and the leading edge sweep is 69°. This geometry has been the subject of numerous numerical studies[10, 16] and was also one of the configurations studied by the NASA Fundamental Aeronautics workshop in 2008[12]. In the SBPW-1 workshop, the simulations were conducted at M_∞ = 1.7 and α = 0°. The available wind tunnel measurements have been extracted at H=24.8 in. and H=31.8 in. for 4 azimuthal angles (0,30,60 and 90°).

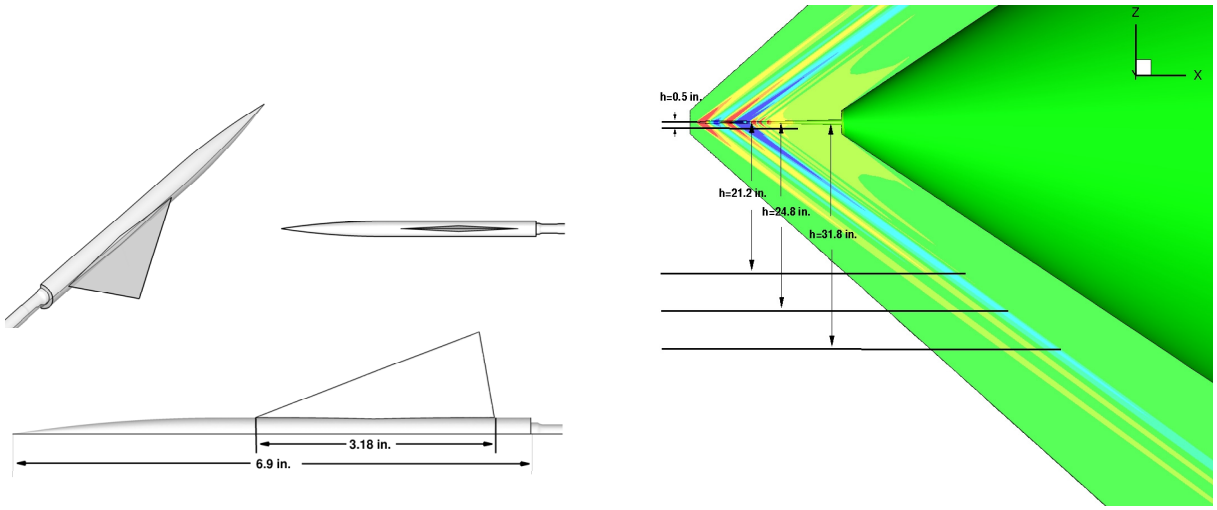

(a) Geometry of DWB **(b) Computation Zone and signal extracted position**

Fig. 8 Geometry and computation zone of DWB

For this test case, Euler simulation results are also presented with the HUNS3D in Euler mode. The tetrahedral meshes are provided by the workshop, with different uniformly refined spaces. The details are shown in table 1.

Table 1 Details of workshop provided tetrahedral mesh

Characteristic Length	2.00s	1.56s	1.25s	1.00s
Cell number	2,830,575	5,877,312	11,451,499	22,727,923

Fig. 9a-b shows the comparison of extracted pressure signal of the Euler computation results with different meshes at various altitudes and Fig. 9c-d with the inclusion of available wind tunnel measured data. The number in the line legend ends with "s" denotes the refined spacing and a smaller number means denser meshes. It is clear that as the mesh refines, there seems to be a slightly higher pressure signal in the shock and expansion wave positions and more details are captured just as the figures show.

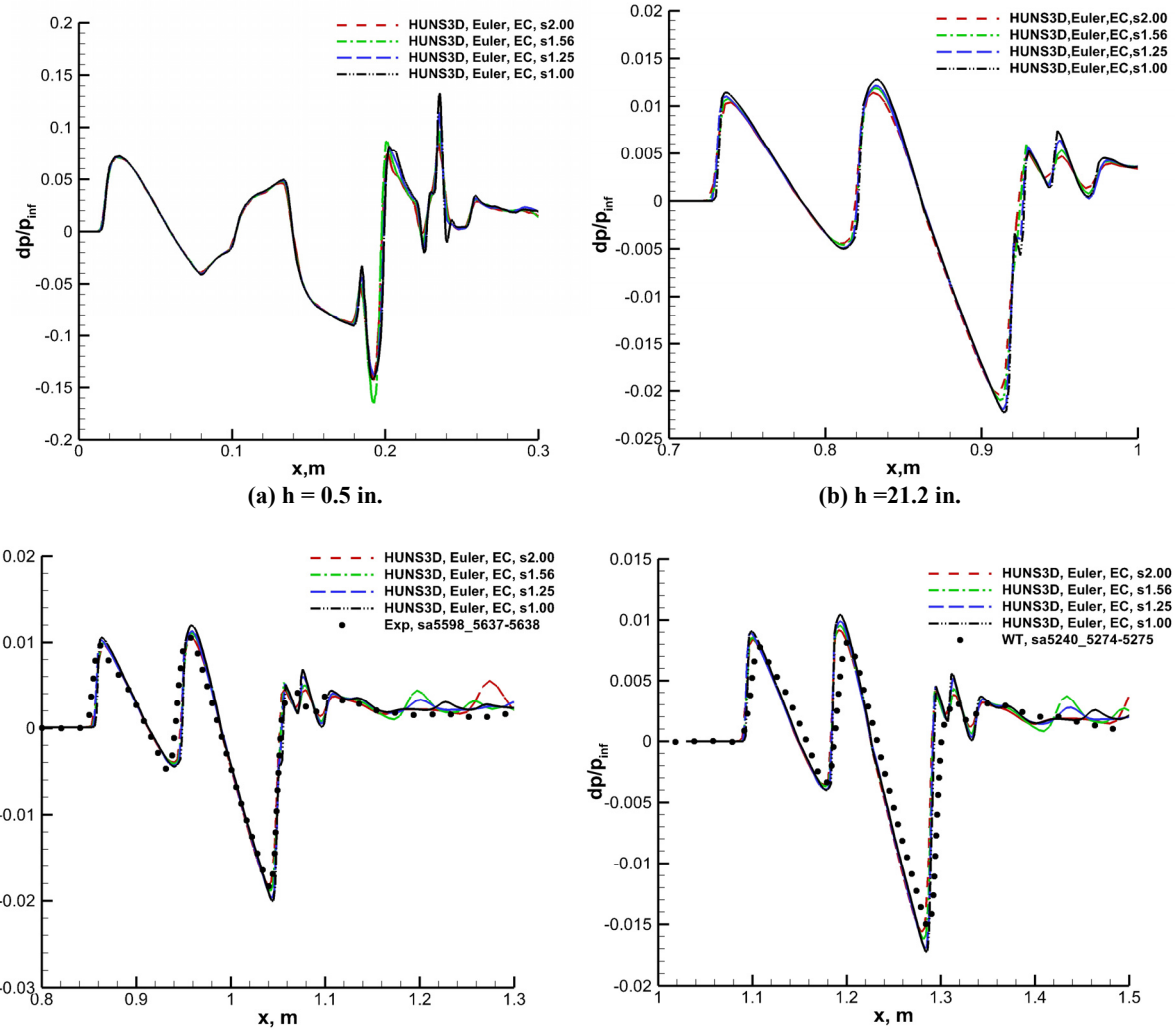

(a) h = 0.5 in. **(b) h =21.2 in.**

(c) h = 24.8 in. **(d) h =31.8 in.**

Fig. 9 Comparison of pressure signal with different Euler mesh

Based on the provided geometry, hybrid unstructured mesh with 7,877,265 cells, 5,525,761 volume nodes, 38,904 surface node points and 39 layers of prism mesh in boundary layer has been generated for viscous computations.

For this model, the simulation with both HUNS3D Euler and HUNS3D NS equations are solved by EC scheme. The entropy production of cube order of shock strength can be produced across the shock by this scheme. This property of EC scheme is considered to be more accurate to capture shock profiles. The computed results of on- and off-track at the altitude of 24.8 in. are compared with experimental measured data in Fig. 10a-d. It is clear that the Euler simulation results have a higher pressure for the forward portion of the signature than the viscous results at the on-track azimuthal angles and off-track azimuthal angles. In addition, the predicted shock location with inviscid method is always behind the NS main shock location. This may be due to the boundary-layer thickness pushing the bow shock wave to a greater shock angle. Besides, the Euler solutions overpredicted almost every peak value of the shockwave and expansion waves, especially in the aft portion. This is mainly caused by the lower numerical dissipation of Euler mode. It can also be noticed that the shock at the aft portion changes from a single to multiple-shock waveform form on-track to off-track.

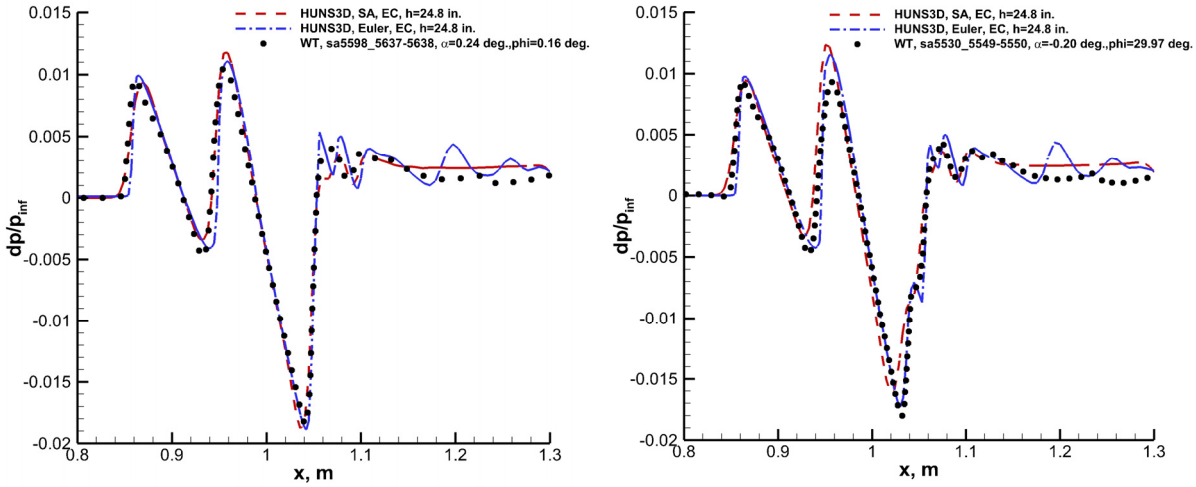

(a) ϕ=0

(b) ϕ=30

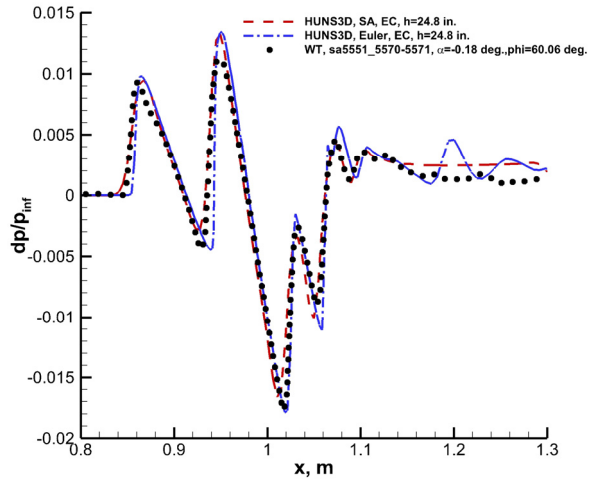

(c) ϕ=60

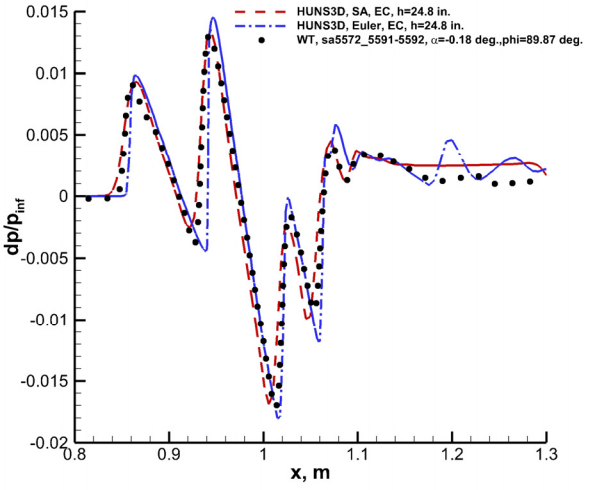

(d) ϕ=90

Fig. 10 69° DWB, HUNS3D turbulent flow Navier-Stokes computation and Euler computations and experiment, M_∞=1.7, α=0°, Re=3.75×10^5, h=24.8 inches

Comparison between the experimental measured data and the on- and off-track computations results at the altitude of 31.8 in. are shown in fig. 11a-d. The result applies the conclusion above.

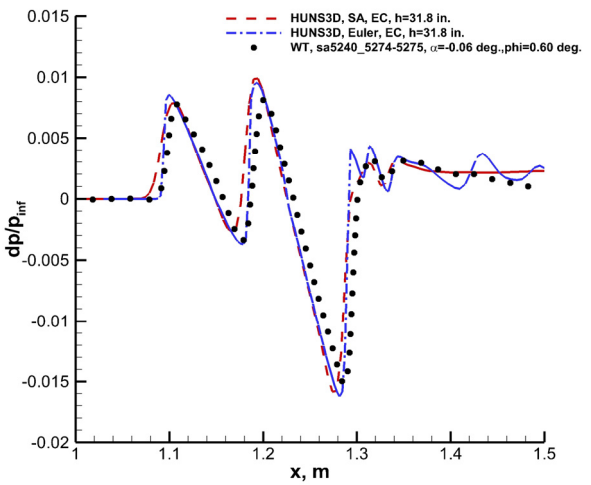

(a) ϕ=0

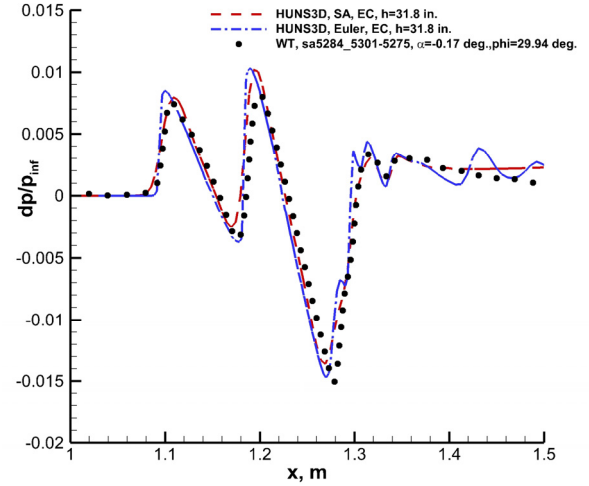

(b) ϕ=30

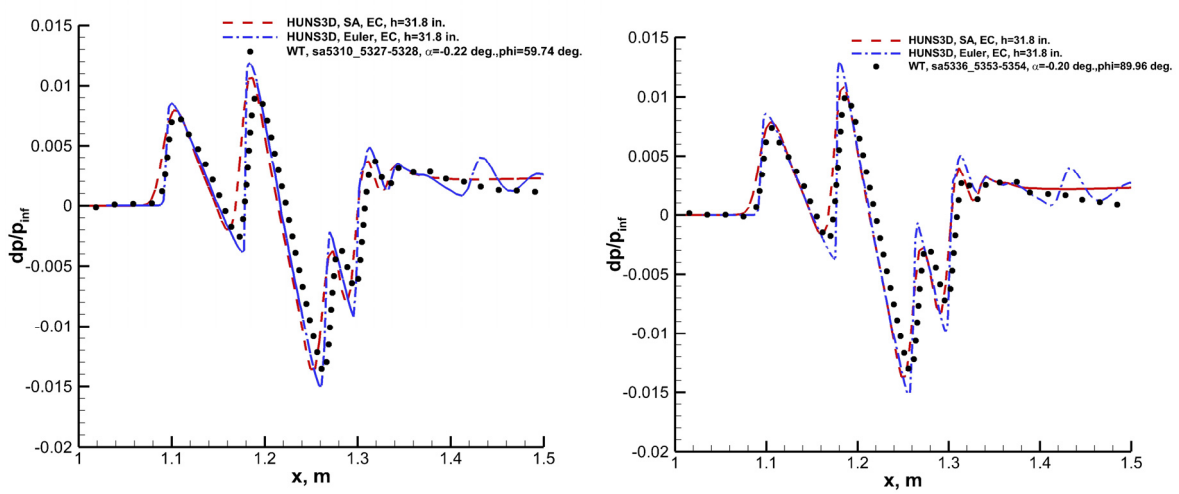

(c) ϕ=60 **(d) ϕ=90**

Fig. 11 69° DWB, HUNS3D turbulent flow Navier-Stokes computation and Euler computations and experiment, M_∞=1.7, α=0°, Re=3.75×10^5, h=31.8 inches

For Seeb-ALR model, we tested the sensitivity of overpressure to the AR in the farfield region, here with DWB model, we tested the sensitivity to the circumferential spacing. Fig. 12 and Fig. 13 show the comparisons between spacing of 8, 4, and 2. The mesh elements increase from 4,844,150 to 8,162,821 as Dtheta decreases from 8 to 2. The results show that the decreasing of the Dtheta would cause sharper shock wave.

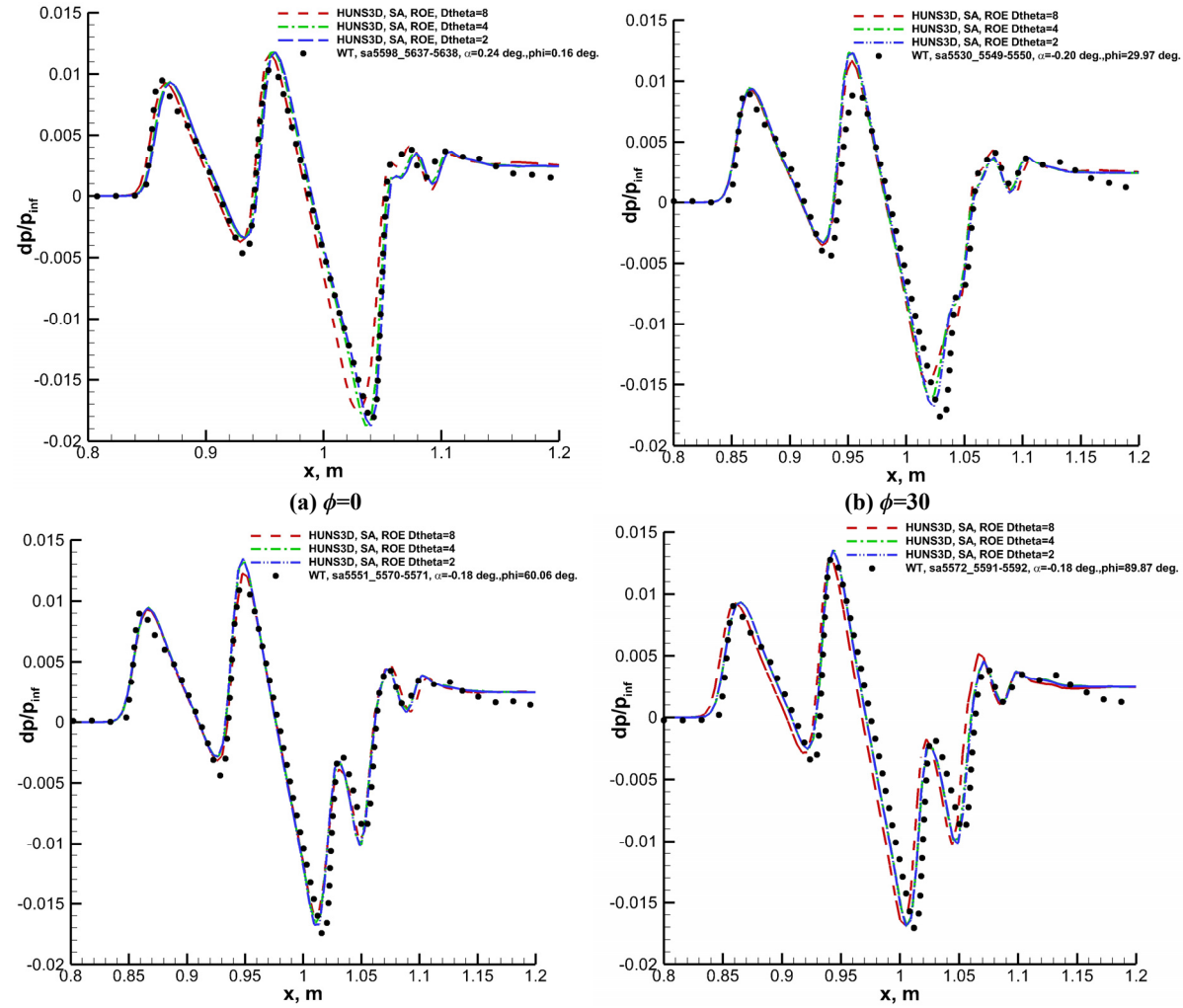

(a) ϕ=0 **(b) ϕ=30**

(c) ϕ=60 **(d) ϕ=90**

Fig. 12 69° DWB, HUNS3D computation and experiment, with different circumferential spacing, **M_∞=1.7, α=0°, Re=3.75×10^5, h=24.8 inches**

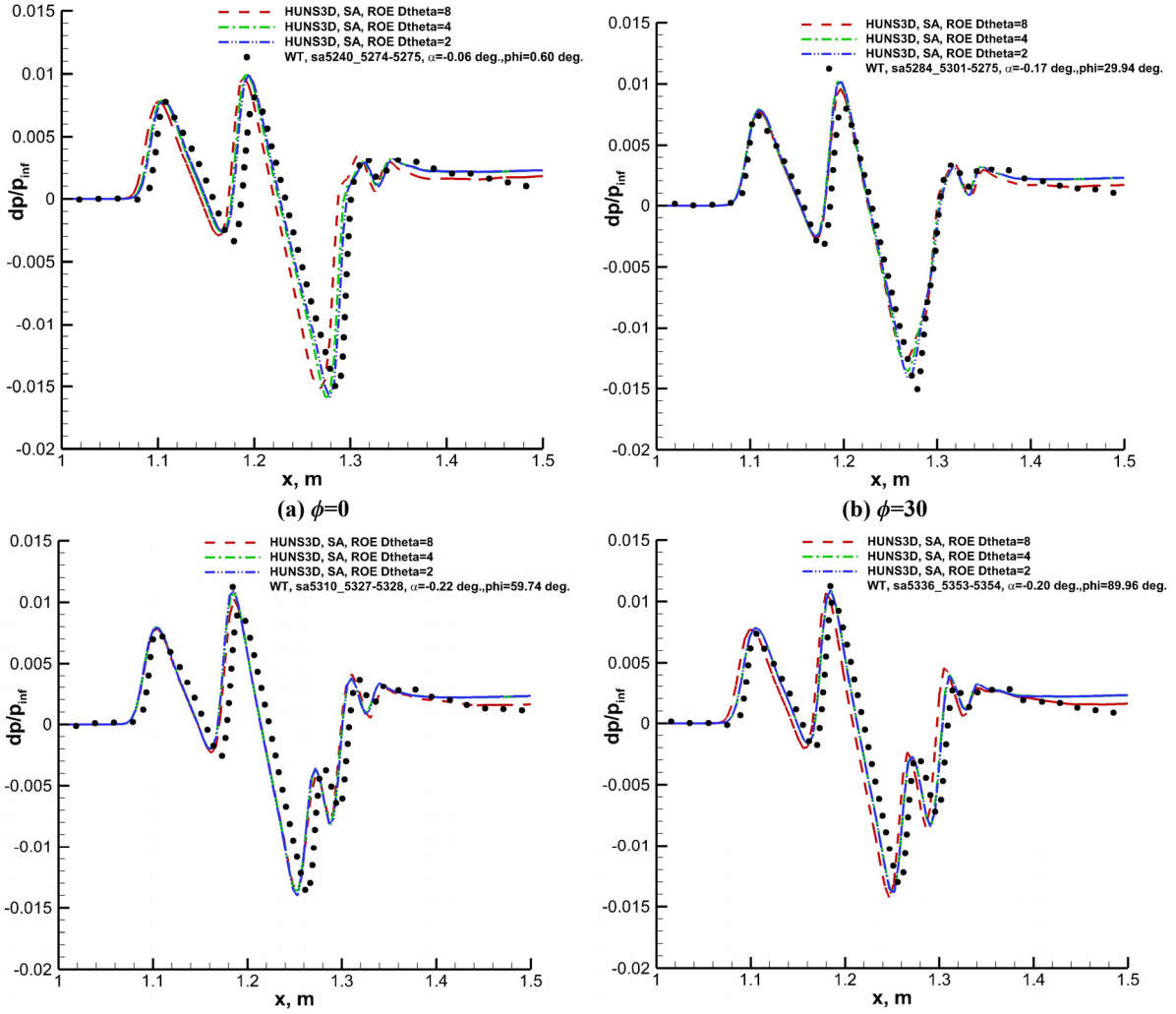

Fig. 13 69° DWB, HUNS3D computation and experiment, with different circumferential spacing**, M_∞=1.7, α=0°, Re=3.75×10^5, h=31.8 inches**

D. LM1021 Model

The LM1021 test case, provided by Lockheed Martin, is a complex full industrial configuration with 3 nacelles, wind dihedral and twin V tails mounted on a blade support to get good aft shock measurement. This low boom concept is the result of many design iterations and was developed as part of the NASA N+2 supersonic validation programs. It was an optional test case for the SBPW-1. The reference length of the model is 22.4 in.. The available signature measurement were tested in NASA Ames 9- by 7-foot wind tunnel at M_∞ = 1.6 and α = 2.3°. The provided geometry had been rotated to the specified incidence, so the simulation should be at 0 degree angle of attack. The geometry and simulation zone is shown in fig14a-b.

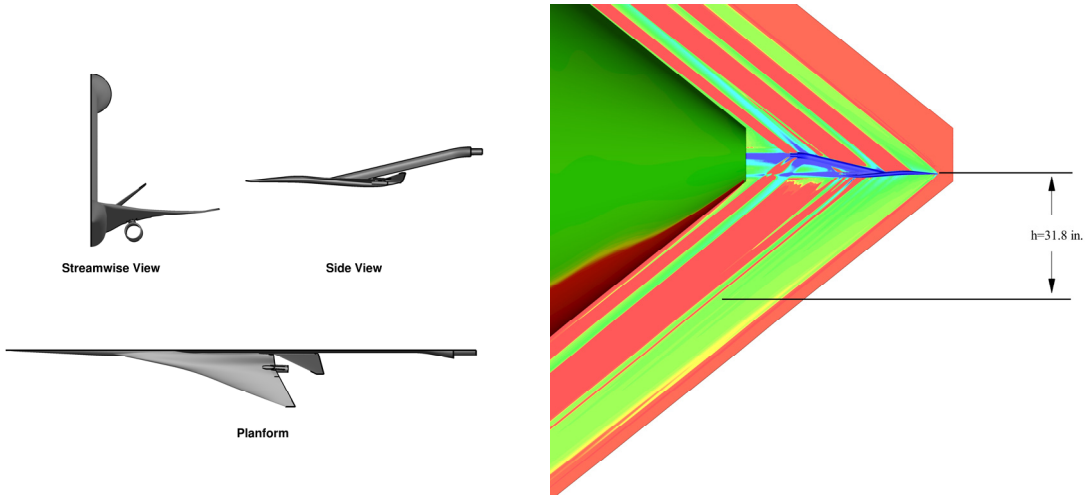

(a) Geometry of LM1021 model **(b) Computation Zone and Extraction Position**

Fig. 14 Geometry and computation zone of LM1021

The unit Reynolds number provided to the SBPW-1 workshop was 2.12E5 per inch, whereas the wind tunnel unit Reynolds number was 3.75E5 per inch,[13, 36] the increase in Reynolds number resulted in improved measurement accuracy and productivity, so in present simulation we set the Reynolds number as 3.75E5.

HUNS3D computations with MSST turbulence and Central schemes are compared with experiment at altitude of 31.8 inches with on and off-track azimuthal angle from 0 to 50 degree in Fig. 15a-f. For the analyses presented herein, second order central differencing along with MSST turbulence were used. The computational comparisons with experimental data are very good with most small pressure oscillations matching the experimental data. However, the pressure in the main expansion is slightly under predicted.

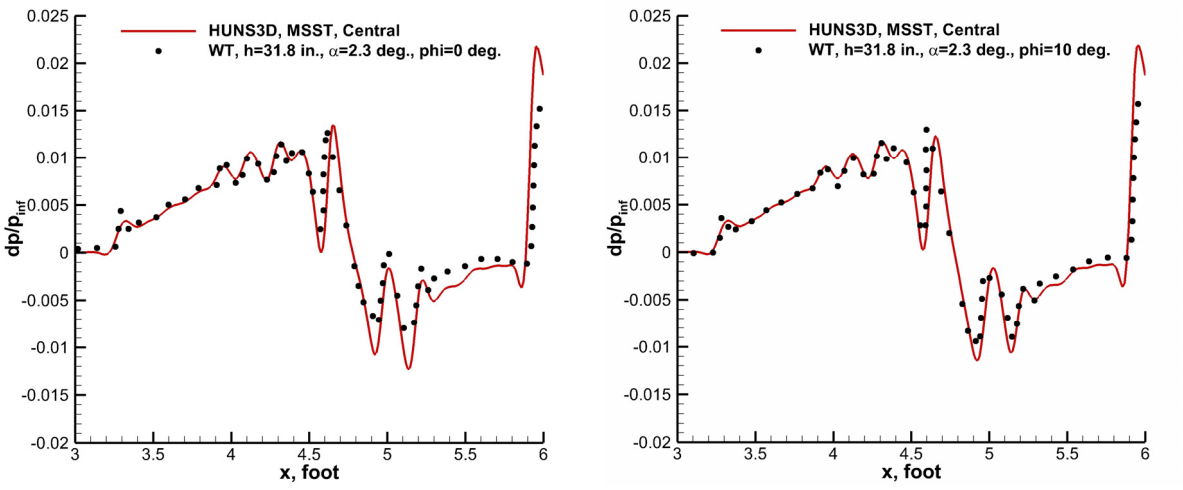

(a) ϕ=0

(b) ϕ=10

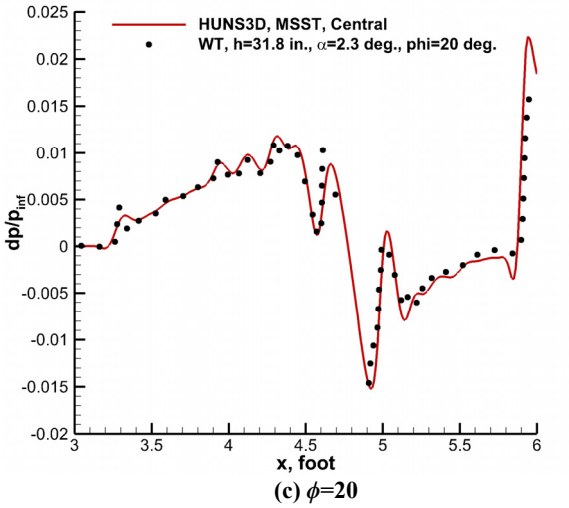

(c) ϕ=20

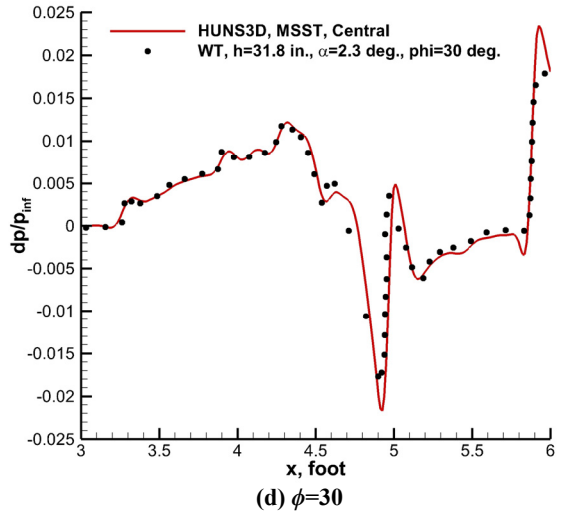

(d) ϕ=30

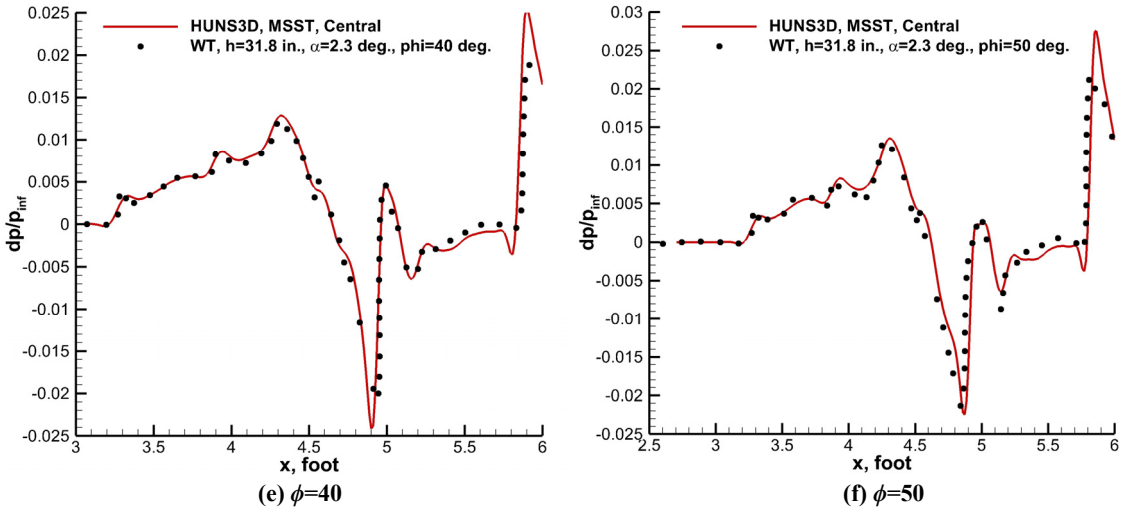

(e) ϕ=40 **(f) ϕ=50**

Fig. 15 LM1021, experimental data compared with HUNS3D computations, M_∞=1.6, α=0°, Re=3.75×10^5, h=31.8 inches

IV. Conclusion

This paper presents the near field sonic boom signature of four benchmark test cases including two axisymmetric bodies, a simple delta wing body and a full configuration includes fuselage, wing, tail, flow-through nacelles, and blade wing. The required and optional cases of the SBPW-1 are all included. The near field sonic boom signature is extracted in 10, 15 and 20 body length below the model for NASA cone and within 2 body length for other 3 models. The CFD simulated results agrees well with the wind tunnel measured data.

The effects of geometry equivalent radius, grid size, turbulence model and spatial discretization schemes are investigated in present paper. Several conclusions can be made based on present work.

1) HUNS3D performs well in sonic boom nearfield sonic boom pressure signature prediction for the present benchmark test cases.
2) The captured shockwave and expansion wave are sensible to geometry bluntness. Results with smaller equivalent radius show better agreement to the experimental data.
3) Turbulence model and spatial discretization schemes have moderate influence in predicting the near field pressure signature.
4) Viscous influence both the shock wave and expansion wave in its position and peak value. The computed results with viscous considered show better agreement to the experimental results than inviscid ones in on and off-track condition.
5) Mesh generation strategy, mesh distribution and cell numbers have obvious influences on near field sonic boom prediction and need to be considered.

V. Acknowledgments

The research was supported by a Chinese foundation numbered 9140A34010214HK03481.

Reference

[1]Alfred Bedard, J. "The Measurement of Sonic Boom Waveforms and Propagation Characteristics - Techniques and Challenges," *13th Aeroacoustics Conference*. AIAA Paper 1990-4004, 1990.

[2]Whitham, G. B. "The Flow Pattern of a Supersonic Projectile," *Communications on Pure and Applied Mathematics*, Vol. 5, No. 3, 1952, pp. 301-348.

[3]Hayes, W. D. "Brief Review of the Basic Theory: Sonic Boom Research," NASA SP147, 1967.

[4]Rallabhandi, S. K. "Advanced Sonic Boom Prediction Using the Augmented Burgers Equation," *Journal of Aircraft*, Vol. 48, No. 4, 2011, pp. 1245-1253.

[5]Cheung, S., Edwards, T., and Lawrence, S. "Application of CFD to Sonic Boom Near and Midfield Prediction," NASA TM 102867, 1990.

[6]Siclari, M. J., and Darden, C. M. "Euler code prediction of near-field to midfield sonic boom pressure signatures," *Journal of Aircraft*, Vol. 30, No. 6, 2015, pp. 911-917.

[7]George, A. R. "Reduction of Sonic Boom by Azimuthal Redistribution of Overpressure," *AIAA Paper 68-159*. Vol. 7, 1968.

[8]Siclari, M. J., and Darden, C. M. "An Euler Code Prediction of Near-field to Midfield Sonic Boom Pressure Signatures," *AIAA Paper 90-4000*. 1990.

[9]Page, J. A., and Plotkin, K. J. "An Efficient Method for Incorporating Computational Fluid Dynamics into Sonic Boom Prediction." Vol. xvi, AIAA Paper 91-3275, 1991, pp. 36-59.

[10]Cliff, S. E., and Thomas, S. D. "Euler/Experiment Correlations of Sonic Boom Pressure Signatures," *Journal of Aircraft*, Vol. 30, No. 5, 1993, pp. 669-675.
[11]Jones, W. T., Nielsen, E. J., and Park, M. A. "Validation of 3D Adjoint Based Error Estimation and Mesh Adaptation for Sonic Boom Prediction - 44th AIAA Aerospace Sciences Meeting and Exhibit (AIAA)," *44th AIAA Aerospace Sciences Meeting and Exhibit*. AIAA Paper 2006-1150, 2006.
[12]Park, M. A., Aftosmis, M. J., Campbell, R. L., Carter, M. B., Cliff, S. E., and Bangert, L. S. "Summary of the 2008 NASA Fundamental Aeronautics Program Sonic Boom Prediction Workshop," *Journal of Aircraft*, Vol. 51, No. 3, 2014, pp. 987-1001.
[13]Park, M. A. a. M., John M. "Summary and Statistical Analysis of the First AIAA Sonic Boom Prediction Workshop," *Journal of Aircraft*, Vol. 53, No. 2, 2016.
[14]Yamashita, R., and Suzuki, K. "Full-Field Simulation for Sonic Boom Cutoff Phenomena," *Transactions of the Japan Society for Aeronautical & Space Sciences*, Vol. 58, No. 6, 2015, pp. 327-336.
[15]Ozcer, I., and Kandil, O. "Fun3D / OptiGRID Coupling for Unstructured Grid Adaptation for Sonic Boom Problems." AIAA Paper 2008-0061, 2008.
[16]Wintzer, M., Nemec, M., and Aftosmis, M. "Adjoint-Based Adaptive Mesh Refinement for Sonic Boom Prediction." AIAA Paper 2008-6593, 2008, pp. 18-21.
[17]Richard, L. C., Melissa, B. C., and Deere, K. A. "Efficient Unstructured Grid Adaptation Methods for Sonic Boom Prediction," *26th AIAA Applied Aerodynamics Conference*. AIAA Paper 2008-7327, 2008.
[18]Aftosmis, J., M., Nemec, Cliff, M. a., and E, S. "Adjoint-Based Low-Boom Design with Cart3D," *29th AIAA Applied Aerodynamics Conference*. AIAA Paper 2011-3500, 2000.
[19]Wintzer, M., and Kroo, I. "Optimization and Adjoint-Based CFD for the Conceptual Design of Low Sonic Boom Aircraft," *Aiaa Aerospace Sciences Meeting Including the New Horizons Forum and Aerospace Exposition*. AIAA Paper 2012-0963, 2012.
[20]Elmiligui, A. A., Cliff, S., Wilcox, F., Nemec, M., Bangert, L., Aftosmis, M. J., and Parlete, E. "Sonic Boom Computations for a Mach 1.6 Cruise Low Boom Configuration and Comparisons with Wind Tunnel Data (Invited)," *29th AIAA Applied Aerodynamics Conference*. AIAA Paper 2011-3496, 2013.
[21]Gan, J., and Zha, G. "Near field Sonic Boom calculation of Benchmark Cases," *53rd AIAA Aerospace Sciences Meeting*. AIAA Paper 2015-1252, 2015.
[22]Mian, H. H., Wang, G., and Raza, M. A. "Application and Validation of HUNS3D Flow Solver for Aerodynamic Drag Prediction Cases," *International Bhurban Conference on Applied Sciences and Technology*. 2013, pp. 209-218.
[23]Roe, P. L. "Approximate Riemann solvers, parameter vectors, and difference schemes," *Journal of Computational Physics*, Vol. 43, No. 2, 1981, pp. 357-372.
[24]Liou, M. S. "Ten years in the making - AUSM-family," *AIAA Journal*, 2013.
[25]Ismail, Farzad, and Philip, L. "Affordable, Entropy-consistent Euler Flux Functions II: Entropy Production at Shocks," *Journal of Computational Physics*, Vol. 228, No. 15, 2009, pp. 5410-5436.
[26]Jameson, A., Schmidt, W., and Turkel, E. "Numerical solution of the Euler equations by finite volume methods using Runge Kutta time stepping schemes." AIAA Paper 81-1259, 1981.
[27]Venkatakrishnan, V. "Convergence to Steady State Solutions of the Euler Equations on Unstructured Grids with Limiters," *Journal of Computational Physics*, Vol. 118, No. 118, 1995, pp. 120-130.
[28]Spalart, P., and Allmaras, S. "A One-equation Turbulence Model for Aerodynamic Flows," *La Recherche Aérospatiale*. AIAA Paper 92-0439, 1992.
[29]Menter, F. R. "Zonal Two Equation k-w Turbulence Models For Aerodynamic Flows," *AIAA Journal*, Vol. 36, No. 11, 1993, pp. 1975-1982.
[30]Li, C., Ye, Z., and Wang, G. "Simulation of Flow Separation at the Wing-Body Junction with Different Fairings," *Journal of Aircraft*, Vol. 45, No. 1, 2008, pp. 258-266.
[31]Park, M. A., Campbell, R. L., Elmiligui, A. A., Cliff, S. E., and Nayani, S. "Specialized CFD Grid Generation Methods for Near-Field Sonic Boom Prediction," *Aerospace Sciences Meeting*. AIAA Paper 2014-0115, 2006.
[32]Carlson, H. W., Mack, R. J., and Morris, O. A. "A Wind-Tunnel Investigation of the Effect of Body Shape on Sonic-Boom Pressure Distributions," NASA TN D-3106, 1965.
[33]Morgenstern, J. M., Buonanno, M., and Marconi, F. "Full Configuration Low Boom Model and Grids for 2014 Sonic Boom Prediction Workshop." AIAA Paper 2013-0647, 2013.
[34]George, A. R., and Seebass, R. "Sonic Boom Minimization Including Both Front and Rear Shocks," *AIAA Journal*, Vol. 9, No. 10, 1971, pp. 2091-2093.
[35]Aftosmis, J., M., and Nemec, M. "Cart3D Simulations for the First AIAA Sonic Boom Prediction Workshop," *52nd Aerospace Sciences Meeting*. AIAA Paper 2014-0558, 2014.
[36]Cliff, S. E., Durston, Donald Chan, William M., Elmiligui, Alaa A., Moiniyekta, Shayan, Sozer, Emre and Jensen, James C. "Computational and Experimental Assessment of Models for the First AIAA Sonic Boom Prediction Workshop," *52nd Aerospace Sciences Meeting*. AIAA Paper 2014-0560, 2014.
[37]Hunton, L. W., Hicks, R. M., and Mendoza, J. P. "Some Effects of Wing Planform on Sonic Boom," NASA TN D-7160, 1973.